A Universal Scaling for the Energetics of Relativistic Jets from Black Hole Systems

R. S. Nemmen,[1]* M. Georganopoulos,[1,2] S. Guiriec,[1] E. T. Meyer,[3,5] N. Gehrels,[1] R. M. Sambruna[4]

Black holes generate collimated, relativistic jets, which have been observed in gamma-ray bursts (GRBs), microquasars, and at the center of some galaxies [active galactic nuclei (AGN)]. How jet physics scales from stellar black holes in GRBs to the supermassive ones in AGN is still unknown. Here, we show that jets produced by AGN and GRBs exhibit the same correlation between the kinetic power carried by accelerated particles and the gamma-ray luminosity, with AGN and GRBs lying at the low- and high-luminosity ends, respectively, of the correlation. This result implies that the efficiency of energy dissipation in jets produced in black hole systems is similar over 10 orders of magnitude in jet power, establishing a physical analogy between AGN and GRBs.

Relativistic jets are ubiquitous in the cosmos and have been observed in a diverse range of black hole systems spanning from stellar mass ($\sim 10 M_\odot$; $M_\odot$, solar mass) to supermassive scales ($\sim 10^5$ to $10^{10} M_\odot$), particularly in the bright flashes of gamma-rays [known as gamma-ray bursts (GRBs)] (*1*, *2*), the miniature versions of quasars lurking in our Galaxy (known as microquasars) (*3*), and active galactic nuclei (AGN) (*4*, *5*). Despite decades of observations at almost all wavelengths and considerable theoretical efforts, many aspects of black hole jets still remain mysterious, such as the mechanism(s) responsible for their formation and the nature of their energetics, as well as their high-energy radiation (*6*, *7*). Jets and outflows from supermassive black holes have important feedback effects on scales ranging from their host galaxies to groups and clusters of galaxies (*8*). Hence, a better understanding of the physics of jets is required to have a more complete picture of the formation and evolution of large-scale structures in the universe and the coevolution of black holes and galaxies (*9*).

One outstanding question is how the jet physics scale with mass from stellar to supermassive black holes. Interestingly, there is evidence to suggest that jets behave in similar ways in microquasars and radio-loud AGN (*10*–*12*). However, a clear connection between AGN and GRBs has not yet been established, though recent work provides encouraging results (*13*, *14*).

As a first step in understanding how the properties of jets vary across the mass scale, we focus on the energetics of jets produced in AGN and GRBs. Therefore, we searched the literature for published and archival observations that allow us to estimate the jet radiative output and the kinetic power for a sample of black hole systems in which the jet is closely aligned with our line of sight and characterized by a broad range of masses. For this reason, our sample consists of blazars—AGNs with their jets oriented

[1]NASA Goddard Space Flight Center, Greenbelt, MD 20771, USA. [2]Department of Physics, University of Maryland Baltimore County, 1000 Hilltop Circle, Baltimore, MD 21250, USA. [3]Department of Physics and Astronomy, Rice University, Houston, TX 77005, USA. [4]Department of Physics and Astronomy, George Mason University, MS 3F3, 4400 University Drive, Fairfax, VA 22030, USA. [5]Space Telescope Science Institute, 3700 San Martin Drive, Baltimore, MD 21218, USA.

*To whom correspondence should be addressed. E-mail: rodrigo.nemmen@nasa.gov

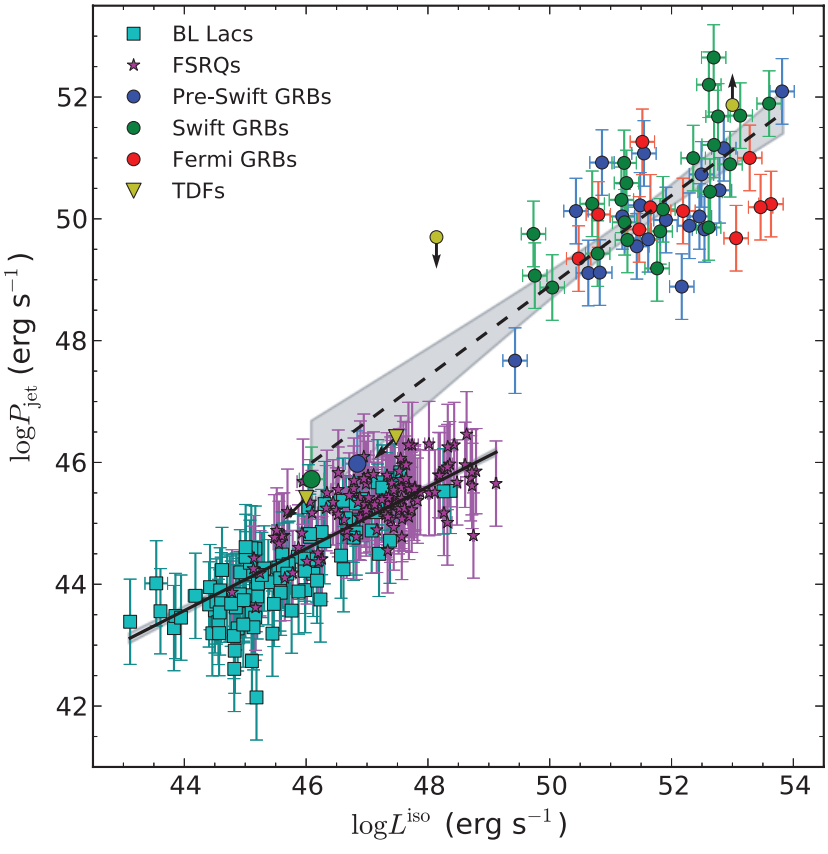

Fig. 1. Relation between the jet kinetic power and the isotropically equivalent gamma-ray luminosity for AGNs and GRBs. Error bars denote 1σ uncertainty. We fitted the two populations separately using a symmetric least-squares method (orthogonal bivariate correlated errors and intrinsic scatter with bootstrapping) (*35*). The blazar and GRB best-fit models correspond to the solid and dashed lines, respectively ($\log P_{\rm jet} = A \log L^{\rm iso} + B$). The best-fit parameters obtained for the blazars are $A = 0.51 \pm 0.02$ and $B = 21.2 \pm 1.1$; for the GRBs, $A = 0.74 \pm 0.08$ and $B = 11.8 \pm 4.1$. The scatter about the best-fit is 0.5 and 0.8 dex for the blazars and GRBs, respectively. The 2σ confidence band of the fits is shown as the gray shaded regions (barely visible for blazars). The two correlations do not agree at the >5σ level. For illustrative purposes, we also include XRF 020903 and GRB 090423 (yellow circles), as well as the two recent tidal disruption flares (TDFs) detected with Swift, which are presumably due to the onset of relativistic jets from the tidal disruption of stars by supermassive black holes (*36*). We do not consider these sources in the statistics, because we only have limits on their luminosities. FSRQs, flat-spectrum radio quasars.

toward Earth (*15*)—and GRBs, the spectral energy distributions of which are completely dominated by the jet due to beaming effects.

As a proxy of the jet bolometric luminosity, we used the observed gamma-ray luminosity L^{iso}, which is isotropically equivalent. To estimate the kinetic power P_{jet}, we use extended radio luminosities for the blazars, whereas for the GRBs we relied on the afterglow measure-

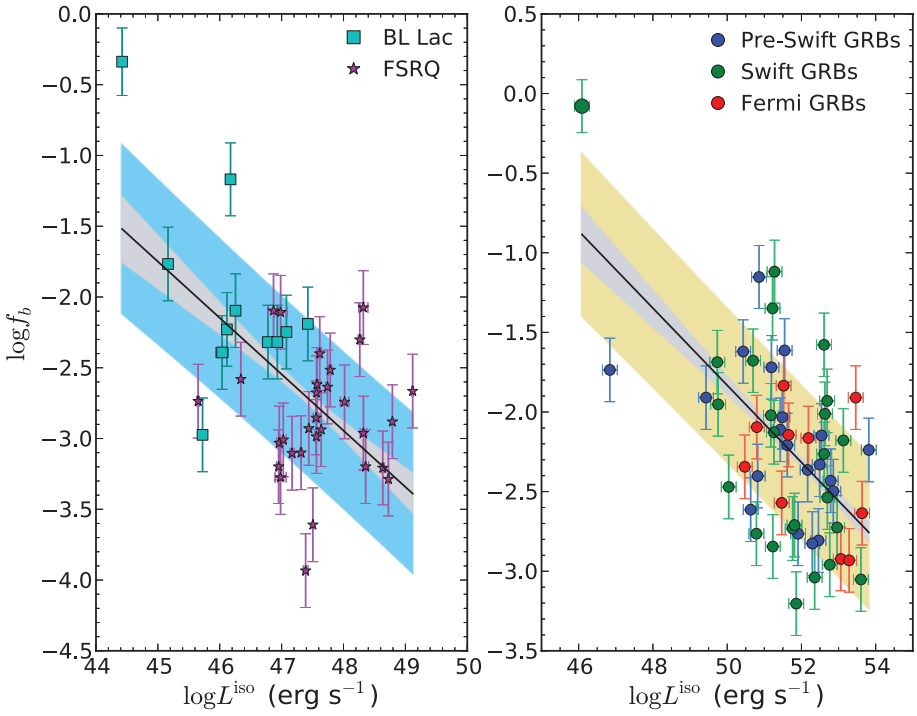

Fig. 2. Relation between the apparent gamma-ray luminosity and the beaming factor for blazars (**left**) and GRBs (**right**). We find correlation coefficient $r = -0.53$ and -0.56 for blazars and GRBs, respectively, indicating anticorrelations significant at the 3.6σ and 4.4σ levels, respectively. The solid lines correspond to the best-fit linear models obtained with the symmetric least-squares fit and are given by $f_b \approx 5 \times 10^{-4}(L_{49}^{iso})^{-0.39 \pm 0.15}$ and $\approx 0.03(L_{49}^{iso})^{-0.24 \pm 0.06}$ for blazars and GRBs, respectively, where $L_{49} \equiv L/10^{49}$. The gray shaded region corresponds to the 1σ confidence band, and the blue and yellow regions are the 1σ prediction bands, which quantify the scatter about the best fits.

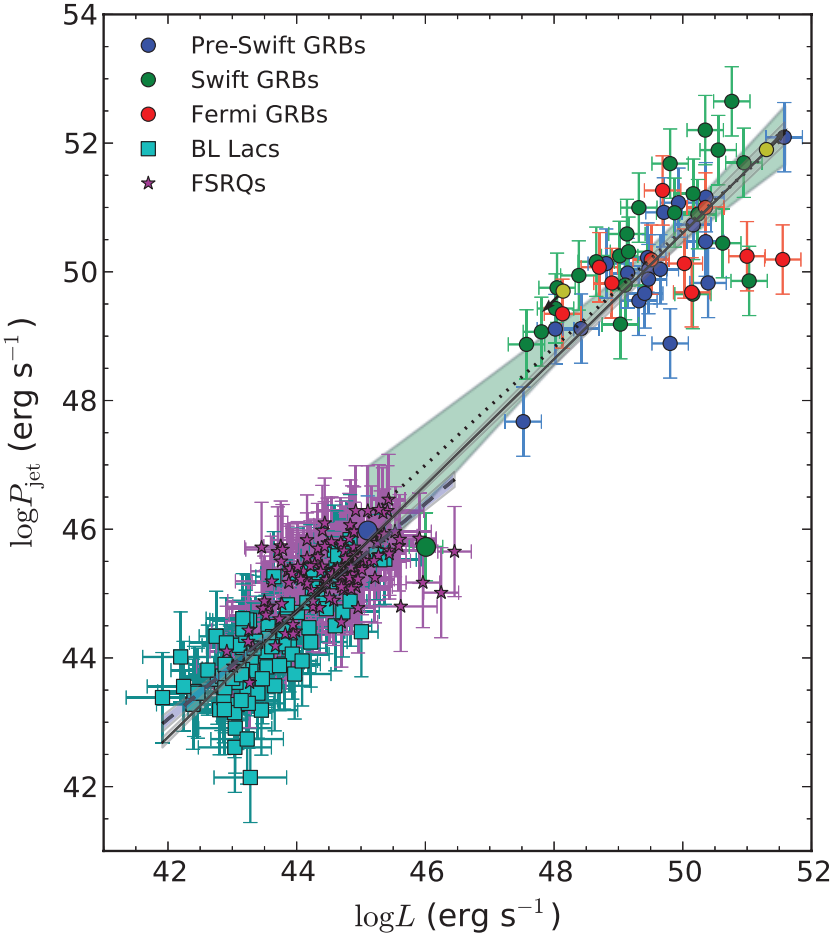

Fig. 3. Relation between the collimation-corrected gamma-ray luminosity $L = f_b L^{iso}$ and the kinetic power for AGNs and GRBs. The shaded regions display the 2σ confidence band of the fits. The blazar and GRB best-fit models (dashed and dotted lines, respectively) follow correlations that are consistent, within the uncertainties, with the best-fit model obtained from the joint data set (solid line). In other words, using L instead of L^{iso} leads to correlations for AGNs and GRBs that are consistent with each other (compare to Fig. 1). The best-fit parameters obtained from the combined data set are $\alpha = 0.98 \pm 0.02$ and $\beta = 1.6 \pm 0.9$, where $\log P_{jet} = \alpha \log L + \beta$. The scatter about the best-fit is 0.64 dex. The yellow data points correspond to XRF 020903 and GRB 090423, which we do not take into account in the statistics.

ments in radio or x-rays. Therefore, the availability of these observables restricted our sample to 234 blazars (106 BL Lacs and 128 flat-spectrum radio quasars) (see table S1) and 54 GRBs (49 long and 5 short GRBs, all with known redshifts z) (see table S2). For blazars, we estimated L^{iso} from the gamma-ray energy flux and the spectral index measured with the Fermi Large Area Telescope (LAT) (*16*). P_{jet} was estimated using an empirical correlation, which relates the Very Large Array (VLA) extended radio emission and the jet kinetic power (*17*, *18*). For GRBs, $L^{iso} = E^{iso}(1 + z)/t_{90}$, where t_{90} is the burst duration and E^{iso} is the isotropically equivalent energy radiated during the prompt emission phase and measured with different telescopes (21 observed with either BeppoSAX, BATSE, HETE, HETE-2, or Integral; 24 with Swift Burst Alert Telescope; and 10 with Fermi). We computed P_{jet} as $P_{jet} = f_b E_k^{iso}(1 + z)/t_{90}$, where E_k^{iso} is the kinetic energy estimated from the radio (VLA) or x-ray (Chandra) luminosity during the afterglow phase using the standard afterglow model (*19*); $f_b \equiv 1 - \cos\theta$ is the "beaming factor"; and θ is the radiation cone half-opening angle, which is the same as the jet opening angle estimated from the jet break in the GRB afterglow light curve (*20*).

We first compared the relative trends of L^{iso} and P_{jet} for the blazar and GRB population separately (Fig. 1). The Pearson correlation coefficients of 0.85 and 0.8 obtained for blazars and GRBs, respectively, indicate a strong correlation within each group of sources. However, the L^{iso}-P_{jet} trend is different for GRBs and blazars, as shown by the fits to the data (Fig. 1).

We computed the intrinsic luminosity L for GRBs and blazars by correcting L^{iso} for the opening angle or beaming factor f_b such that $L = f_b L^{iso}$. For GRBs, the beaming factor is computed from the jet opening angle θ_j as $1 - \cos\theta_j$ (*21*); for blazars, f_b is estimated as $1 - \cos 1/\Gamma$, where Γ is the bulk Lorentz factor of the flow, because AGNs obey $\theta_j < 1/\Gamma$ (*22*, *23*). Although an estimate of θ_j is available for each GRB in the sample, Γ is only available for a subset of 41 blazars. Figure 2 shows an anticorrelation between L^{iso} and f_b for both GRBs and blazars with compatible indices when fit with a power law. Because θ is not available for the whole blazar sample, we used the power-law fit of L^{iso} versus f_b as an estimator for f_b.

As with L^{iso} and P_{jet}, L and P_{jet} are strongly correlated within the GRB and AGN samples (Fig. 3). However, they follow the same trend within the narrow uncertainties and the whole GRB and blazar sample can be fit adequately with a power law over 10 orders of magnitude in luminosity. Therefore, the relativistic jets in GRBs and blazars are consistent with obeying the relation $P_{jet} \approx 4.6 \times 10^{47}(L/10^{47})^{0.98}$ erg s^{-1}, within the measurement uncertainties. In other words, once "black hole engines" produce relativistic jets, they seem to do so maintaining the same coupling between the total power carried by the jet and power radiated away. This universal scaling for the energetics of jets is maintained across the mass scale, regardless of the different environments and accretion flow conditions around the compact object.

Figure 4 indicates that most of the jets in our sample dissipate at least 3% of the power carried by the jet as radiation, and overall, they can radiate as much as 15%. This range of efficiencies is considerably higher than previous estimates for AGNs based on radio to x-ray luminosities (*24*, *25*), but our results are in agreement with those obtained from blazar broadband spectral models (*26*, *27*), as well as GRB afterglow studies (*28*–*30*). Efficient heating of electrons seems to be a universal property of relativistic magnetized shocks according to numerical simulations (*31*), which demonstrate that electrons retain ≳15% of the preshock energy. If most of the postshock energy is radiated away, these theoretical results could pave the way to an understanding of the high dissipation efficiencies that we find.

Our results suggest that there is a single fundamental mechanism to produce relativistic jets in the universe. The analogy known to exist between microquasars and AGNs (*3*, *10*, *11*) can be extended to the gamma-ray bursts with the fundamental difference that, whereas AGNs and microquasars undergo recurrent activity, GRBs experience only one episode of hyperaccretion.

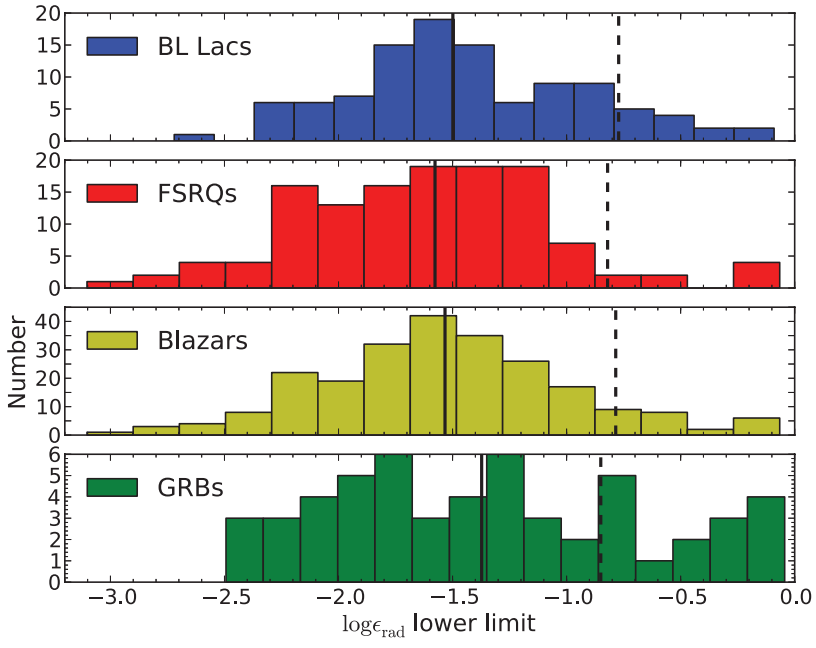

Fig. 4. Distribution of the 1σ lower limits on the jet radiative efficiency (the fraction of the total jet power that is converted to gamma rays) $\epsilon_{rad} \equiv L/(L + P_{jet})$ for AGNs and GRBs. The vertical solid lines indicate the median values of the lower limits; the dashed lines represent the median values of ϵ_{rad} for each sample. Most of the sources are characterized by $\epsilon_{rad} > 3\%$. The median efficiencies correspond to ~15%, considering that these estimates are affected by ~0.5 to 0.7 dex uncertainties, on average.

References and Notes

1. N. Gehrels, E. Ramirez-Ruiz, D. B. Fox, *Annu. Rev. Astron. Astrophys.* **47**, 567 (2009).
2. T. Piran, *Rev. Mod. Phys.* **76**, 1143 (2005).
3. I. F. Mirabel, L. F. Rodriguez, *Annu. Rev. Astron. Astrophys.* **37**, 409 (1999).
4. M. J. Rees, *Annu. Rev. Astron. Astrophys.* **22**, 471 (1984).
5. J. H. Krolik, *Active Galactic Nuclei: From the Central Black Hole to the Galactic Environment* (Princeton Univ. Press, Princeton, NJ, 1999).
6. D. L. Meier, S. K. Koide, Y. Uchida, *Science* **291**, 84 (2001).
7. R. Narayan, E. Quataert, *Science* **307**, 77 (2005).
8. B. McNamara, P. E. J. Nulsen, *Annu. Rev. Astron. Astrophys.* **45**, 117 (2007).
9. D. Sijacki, V. Springel, T. Di Matteo, L. Hernquist, *Mon. Not. R. Astron. Soc.* **380**, 877 (2007).
10. A. P. Marscher *et al.*, *Nature* **417**, 625 (2002).
11. A. Merloni, S. Heinz, T. Di Matteo, *Mon. Not. R. Astron. Soc.* **345**, 1057 (2003).
12. H. Falcke, E. Körding, S. Markoff, *Astron. Astrophys.* **414**, 895 (2004).
13. J. Wang, J. Y. Wei, *Astrophys. J.* **726**, L4 (2011).
14. Q. Wu, Y.-C. Zou, X. Cao, D.-X. Wang, L. Chen, *Astrophys. J.* **740**, L21 (2011).
15. M. Ulrich, L. Maraschi, C. M. Urry, *Annu. Rev. Astron. Astrophys.* **35**, 445 (1997).
16. M. Ackermann *et al.*, *Astrophys. J.* **743**, 171 (2011).
17. E. T. Meyer, G. Fossati, M. Georganopoulos, M. L. Lister, *Astrophys. J.* **740**, 98 (2011).
18. K. W. Cavagnolo *et al.*, *Astrophys. J.* **720**, 1066 (2010).
19. D. L. Freedman, E. Waxman, *Astrophys. J.* **547**, 922 (2001).
20. See supplementary materials for more details.
21. D. A. Frail *et al.*, *Astrophys. J.* **562**, L55 (2001).
22. S. G. Jorstad *et al.*, *Astron. J.* **130**, 1418 (2005).
23. A. B. Pushkarev, Y. Y. Kovalev, M. L. Lister, T. Savolainen, *Astron. Astrophys.* **507**, L33 (2009).
24. A. Celotti, A. Fabian, *Mon. Not. R. Astron. Soc.* **264**, 228 (1993).
25. F. Yuan, Z. Yu, L. C. Ho, *Astrophys. J.* **703**, 1034 (2009).
26. A. Celotti, G. Ghisellini, *Mon. Not. R. Astron. Soc.* **385**, 283 (2008).
27. G. Ghisellini *et al.*, *Mon. Not. R. Astron. Soc.* **402**, 497 (2010).
28. Y. Fan, T. Piran, *Mon. Not. R. Astron. Soc.* **369**, 197 (2006).
29. B. Zhang *et al.*, *Astrophys. J.* **655**, 989 (2007).
30. J. L. Racusin *et al.*, *Astrophys. J.* **738**, 138 (2011).
31. L. Sironi, A. Spitkovsky, *Astrophys. J.* **726**, 75 (2011).

32. D. N. Burrows *et al.*, *Nature* **476**, 421 (2011).
33. S. B. Cenko *et al.*, *Astrophys. J.* **753**, 77 (2012).
34. J. S. Bloom *et al.*, *Science* **333**, 203 (2011).
35. M. G. Akritas, M. A. Bershady, *Astrophys. J.* **470**, 706 (1996).
36. To include the tidal disruption flares in Fig. 1, we used the Fermi LAT upper limit (*32*) observed for Swift J164449.3+573451, and we assumed $L^{iso} \sim L_X$ for Swift J2058.4+0516 (*33*), where L_X is the observed x-ray luminosity. We assumed $P_{jet} \sim L_{Edd}$, where L_{Edd} is the Eddington luminosity based on the black hole masses estimated in (*32*–*34*). These luminosities and powers should be treated as upper limits.

Acknowledgments: We thank J. Racusin, M. Lister, C. Dermer, A. Pushkarev, J. McEnery, D. Donato, D. Kazanas, T. Nelson, and F. Tombesi for crucial discussions. R.S.N. and S.G. were supported by an appointment to the NASA Postdoctoral Program at Goddard Space Flight Center, administered by Oak Ridge Associated Universities through a contract with NASA. This research has made use of: (i) StatCodes statistical software hosted by The Pennsylvania State University's Center for Astrostatistics; (ii) data obtained from the HETE science team via the Web site http://space.mit.edu/HETE/Bursts/Data (HETE is an international mission of the NASA Explorer program, run by the Massachusetts Institute of Technology); and (iii) NASA/IPAC Extragalactic Database (NED), which is operated by the Jet Propulsion Laboratory, California Institute of Technology, under contract with NASA.

Supplementary Materials
www.sciencemag.org/cgi/content/full/338/6113/1445/DC1
Supplementary Text
Fig. S1
Tables S1 to S4
References (*37*–*75*)

13 July 2012; accepted 1 November 2012
10.1126/science.1227416

Texture of Nanocrystalline Nickel: Probing the Lower Size Limit of Dislocation Activity

Bin Chen,[1,2]* Katie Lutker,[3] Selva Vennila Raju,[1,2,4] Jinyuan Yan,[1,2] Waruntorn Kanitpanyacharoen,[5] Jialin Lei,[6] Shizhong Yang,[6] Hans-Rudolf Wenk,[5] Ho-kwang Mao,[7,8] Quentin Williams[2]

The size of nanocrystals provides a limitation on dislocation activity and associated stress-induced deformation. Dislocation-mediated plastic deformation is expected to become inactive below a critical particle size, which has been proposed to be between 10 and 30 nanometers according to computer simulations and transmission electron microscopy analysis. However, deformation experiments at high pressure on polycrystalline nickel suggest that dislocation activity is still operative in 3-nanometer crystals. Substantial texturing is observed at pressures above 3.0 gigapascals for 500-nanometer nickel and at greater than 11.0 gigapascals for 20-nanometer nickel. Surprisingly, texturing is also seen in 3-nanometer nickel when compressed above 18.5 gigapascals. The observations of pressure-promoted texturing indicate that under high external pressures, dislocation activity can be extended down to a few-nanometers-length scale.

The plastic behavior of coarse-grained metals (with particle size >100 nm) is mainly controlled by the nucleation and motion of lattice dislocations. Plastic deformation by dislocation glide results in crystallite rotations, generating lattice-preferred orientation or texture. The anisotropic physical properties of a polycrystalline material are strongly related to the preferred alignment of its crystallites. In material science and engineering, texture control is essential in improving the strength and lifetime of structural materials (*1*). In Earth science, understanding texture development of minerals is important for interpreting seismic anisotropy in Earth's interior (*2*).

How plastic deformation occurs in nanocrystalline materials remains controversial (*3*–*15*). Post-deformation analysis of compressed or indented nanocrystalline nickel does not indicate major dislocation debris (*12*), whereas dislocations are observed in 10-nm nickel and 9-nm platinum particles (*13*, *14*). Deformation twinning and disclination have also been reported in several studies on nanocrystals (*6*, *9*–*11*, *15*). Although it is commonly believed that the intrinsic deformation behavior of nanomaterials arise from the interplay between defects and grain-boundary (GB) processes (*11*, *16*), the precise trade-offs between these deformation mechanisms are still unclear, as is the effect of pressure on these different mechanisms. It has been proposed that below a critical length scale, the strength of nanometals would exhibit an inverse Hall-Petch size dependence because in the plastic deformation of fine nanocrystals, dislocation activity gives way to GB sliding, diffusion, and grain rotation (*4*, *5*). In contrast, twin thickness has been found to affect the maximum strength of copper, implying that the plastic deformation of nanomaterials is not necessarily related to GB-mediated processes (*9*). Indeed, it has been proposed that dislocation nucleation governs material softening in nano-twinned metals (*10*).

Because of technical limitations, in situ observation of plastic deformation in ultrafine nanocrystals is difficult, precluding the direct exploration of mechanics at nanometer scales. Whether plasticity in ultrafine nanocrystals is still generated by dislocations, how pressure affects the deformational regimes of nanoparticles, and how structural anisotropy is affected by size reductions are all unresolved questions. The effect of pressure on dislocations is complex in terms of both the high-pressure energetics of dislocation cores and their mobilities, with the net overarching effects of pressure being unclear (*17*). It has been observed that at high pressure, brittle materials such as oxides and silicates become ductile, even at room temperature (*2*). Our goal is to examine the interplay between pressure and particle size in determining when dislocation-mediated deformation processes predominate within nanoparticles and, correspondingly, what the lower size limit of dislocation activity is. In this work, radial diamond anvil cell (rDAC) x-ray diffraction (XRD) experiments (*2*) were used to make in situ observation of the texturing in stressed polycrystalline nickel of various mean particle sizes, from 500 nm down to 3 nm.

We deformed the nickel samples plastically in rDACs (fig. S1) (*18*). The XRD experiments were performed at beamline 12.2.2, Advanced Light Source (ALS), Lawrence Berkeley National Laboratory. The particle sizes of the nickel samples are 500 ± 45 nm, 20 ± 8 nm, and 3 ± 0.9 nm (fig. S2) (*18*), respectively. The relatively narrow size distributions allow the investigation of the size dependence of texturing. When shear stress is applied to polycrystals, individual crystals deform preferentially on slip planes. This results in crystal rotations that in turn lead to texture development (*1*). The radial diffraction images show variations in diffraction peak position with respect to the compression direction, indicating differential stresses in the material. They also display systematic intensity variations that can be used to deduce texture (Fig. 1 and figs. S3 to S6) (*18*). For instance, the diffraction intensity of the 500-nm nickel at 5.0 GPa is minimal in the compression direction for the (200) diffraction peak but maximal for the (220) peak (fig. S3). Diffraction intensity variations are seen in the 500-nm nickel above 3.0 GPa and in 20-nm nickel above 11.0 GPa, and more modest but resolvable intensity variations are observed in 3-nm nickel at pressures above 18.5 GPa. The variations in diffraction intensity can be best seen in the "unrolled diffraction" images recorded as a function of diffraction angle (Fig. 1).

[1]Advanced Light Source, Lawrence Berkeley National Lab, Berkeley, CA 94720, USA. [2]Department of Earth and Planetary Sciences, University of California, Santa Cruz, Santa Cruz, CA 95064, USA. [3]Department of Chemistry, University of California, Berkeley, Berkeley, CA 94720, USA. [4]Department of Physics, University of Nevada, Las Vegas, NV 89119, USA. [5]Department of Earth and Planetary Science, University of California, Berkeley, Berkeley, CA 94720, USA. [6]Louisiana Optical Network Initiative (LONI) Institute, Southern University, Baton Rouge, LA 70813, USA. [7]Geophysical Laboratory, Carnegie Institution of Washington, Washington, DC 20015, USA. [8]Center for High Pressure Science and Technology Advanced Research, Shanghai 201203, China.

*To whom correspondence should be addressed. E-mail: bchen@lbl.gov

A Universal Scaling for the Energetics of Relativistic Jets from Black Hole Systems

R. S. Nemmen, M. Georganopoulos, S. Guiriec, E. T. Meyer, N. Gehrels and R. M. Sambruna

Science **338** (6113), 1445-1448.
DOI: 10.1126/science.1227416

So Different Yet So Similar

Gamma-ray bursts (GRBs) are associated with the collapse of stars into black holes. Blazars are a class of active galaxies powered by accretion onto central black holes with masses a million to a billion times that of the Sun. **Nemmen *et al.*** (p. 1445) show that, despite tremendous differences in luminosity and black hole mass, the relativistic jets produced in GRBs and blazars follow the same correlation between the kinetic power carried by the accelerated particles and the energy radiated away in the jet, suggesting that there may be a single mechanism for producing relativistic jets.